International Journal of Impact Engineering 114 (2018) 169–181

Contents lists available at ScienceDirect

International Journal of Impact Engineering

journal homepage: www.elsevier.com/locate/ijimpeng

Laboratory scale investigation of stress wave propagation and vibrational characteristics in sand when subjected to air-blast loading

Padmanabha Vivek*, Thallak G. Sitharam

Department of Civil Engineering, Indian Institute of Science, Bangalore, India

ARTICLE INFO

Keywords:
Air-blast
Shock tube
Sand

ABSTRACT

The main objective of this study is to develop a new approach for evaluating the effects of air-blast on protective barrier made of sand. The air-blast loading is simulated experimentally laboratory using the shock tube test facility. The stress wave propagation in medium dense and dense sand medium are investigated under simulated air-blast loading. Synchronised pressure and accelerometer measurement system is used to capture peak stress wave pressure and peak particle velocity (PPV). The blast wave impact generates a stress wave in the medium leading to the compaction of the soil skeleton, which has led to stress enhancement (4–5 times of peak over-pressure) in top most sand layer, following which the high-pressure gas behind the shock front permeates through the sample. The intensity of stress waves and gas permeation rate gradually decrease with depth. Further, from the result of the simulated air-blast experiments, an empirical equation has been developed with a power law index of 1.88 and 1.36 for medium dense and dense sand respectively, to predict PPV against scaled blast distance. Visualisation of the sand deformation was possible with the help of a high-speed camera; displacement trajectories and strain contours are obtained through digital image correlation (DIC) analyses.

1. Introduction

For over a century, sand bags are commonly used in the war fields to mitigate the blast effects. Till date, sand is proved to be an excellent energy absorbent material and is efficiently used as protective barriers against sudden impact and blast loadings. Sandbags are commonly used around the trenches and the bunkers, which act as a temporary fortification and a base for underground storages against the possible air strikes [1,2]. Regardless of the fortification material, the roof surface is covered with a layer of sand intended for shock absorption. In certain cases, the entire bunker will have sandbagged roof. Sand layer is also used as a base isolation system to mitigate the ground shock effects on structures, resulting from the blast loads [3].

Very little is known about the dynamic response of sand during air-blast impact loading. However, numerous studies have been reported on the dynamic behaviour of soil when subjected to underground and surface blast conditions. Among them, a few relevant papers which discusses the propagation of dynamic wave in the surrounding soils are listed: Alekseenko and Rykov [4]; William and Robert [5]; Drake and Little [6]; TM5-855-1 [7]; Rinehart and Welch [8]; Roy [9]; Wu et al. [10]. Under purview of shock wave propagation in sands, researchers [11–17] have carried out extensive studies at high pressure and high strain rate. Several empirical equations[18–20] have been developed as a function of buried explosive mass and distance, to predict parameters like peak soil pressure (PSP) and peak particle velocity (PPV). The parameters are generally represented as a function of scaled distance and is commonly represented in the form, as shown below.

$$PSP/PPV = C.\ (Z)^{-k} \tag{1}$$

$$Z = \frac{H}{W^{\frac{1}{3}}} \tag{2}$$

where, 'Z' is scaled distance, 'W' is charge weight, 'H' is distance measured from source of explosion, 'C' is a material constant and the exponent term is termed as attenuation coefficient (k). The 'k' value predicted for the PPV for the buried blast condition in case of dry loose and dense sand deposit is reported to be 3 and 2.5 respectively [21].

Only a few literatures are available which studies the effect of explosion in air on the soils. A series of field experiments with TNT charges of 1, 2, 4, 7 and 10 kg of TNT, at 0.5 m and 1 m above the ground level, have been conducted by Ambrosini et al. [22]. The aim of their experiment was to address the crater formation phase of an air-blast event. Similar small scale experiments on a clayey soil deposit using TNT was performed by Busch et al. [23]. Seismograph signals obtained from the buried geophones and air-blast sensors were used to obtain a relationship for ground vibration and crater dimension, with

* Corresponding author.
E-mail addresses: vivekp@iisc.ac.in (P. Vivek), sitharam@iisc.ac.in (T.G. Sitharam).

https://doi.org/10.1016/j.ijimpeng.2018.01.003
Received 3 June 2017; Received in revised form 28 December 2017; Accepted 3 January 2018
Available online 04 January 2018
0734-743X/

the explosive mass and distance from the ground surface. The above-mentioned studies have primarily focused on impact crater formation and the information available on the ground vibration is very much limited to the cohesive soil deposit. Moreover, no results are available on the shock pressure attenuation and stress distribution in the soil during blast impact. However, there is considerable data available on the shock attenuation behaviour of sand. Most of the test data are obtained from the laboratory studies using shock tubes. One of the earliest attempts was made by Akai et al. [24] to investigate the dynamic behaviour of soils due to shock loading. The attenuation of peak stress, in confined sandy loam, indicated an exponential decay. Van der Grinten et al. [25] and others [26,27] have observed similar behaviour of pressure amplitudes in dry and wet sand media. Ben-Dor et al. [28] has performed experiments on various types of granular materials (potash, polysterene, nylon, sand etc.). The rise in the pressure is attributed to two phenomena: compaction of the granular particles due to the shock impact and gas filtration, which affects the particles by the drag forces between the solid and gaseous phases. The gas filtration process was extensively studied by Britan et al. [29] using natural quartz sand. Vivek and Sitharam [30] have performed shock tube experiments on the geotextile encapsulated sand barrier units (analogous to sand bags) against shock impact loads. In most of the studies mentioned above, pressure pulse generated by shock tube has a constant pressure zone behind the shock front and the impulse generated will be significantly different from that of an air blast wave. Blast wave impulses depend, not only on the peak overpressure and the duration of the wave, but also on the rate of decay of the overpressure [19]. Overall, these studies have provided limited information on the attenuation performance of sand medium with reference to air-blast. In addition to shock pressure attenuation, further investigation on air-blast is necessary to obtain vibrational response parameters, such as, peak particle acceleration (PPA), peak particle velocity (PPV) and the strain induced in the sand medium.

Field blast tests using explosives are very expensive and large number of tests have to be performed, since repeatability is difficult to achieve in field blast testing [31]. Alternatively, the tests are performed in the laboratory, in a controlled manner, using a blast wave simulator like shock tube.

In the present study, air-blast wave is simulated using compressed gas driven shock tube. The primary objective of this study is to provide an insight into the spatial distributions of particle velocity and pressure over the sand specimen, impacted by blast waves. This article will provide some quantitative information regarding the magnitude of shock pressure and vibrational amplitudes, in medium dense and dense sand deposits. The above aspects are addressed in three stages: (i) the propagation and attenuation of stress waves, (ii) acceleration and velocity response of sand particles and (iii) dynamic strains induced in sand medium. To gain a better understanding of the response of sand, experiments are performed for different blast wave intensities.

2. Experimental setup

The experimental setup is broadly categorised into three major sections: shock tube, test chamber and appropriate instrumentation system (which includes both contact and non-contact based measurement techniques).

2.1. Shock tube

A shock tube is a long cylindrical tube which essentially consists of two sections: (i) the driver section, the one which contains high-pressure gas and (ii) the driven section, which is kept at a relatively lower pressure. The schematic diagram of the twin-shock tube used in the present study is shown in Fig. 1(a). Twin-shock tube features two identical shock tubes (L and R) mounted on a common platform and the exit of the tubes is connected to a large cylindrical dump tank, where the samples are located. The total length of the shock tube is 5 m and the internal diameter is 135 mm. The driver and the driven sections are made up of customised modular units of 0.5 m and are separated by a metal diaphragm, which is housed in the diaphragm mounting section. The metal diaphragms generally have a v-groove, which would facilitate them to rupture in a controlled manner, with repeatable bursting pressures. Blast waves of different intensities are obtained by bursting diaphragms of different thickness.

The experiments in the present study are performed using the shock tube-(R), with the following test configuration: (i) driver length of 0.5 m (ii) driven length of 4.5 m and (iii) three different aluminium diaphragms of thickness 5 mm, 4 mm and 2 mm with groove depths of 2 mm, 1 mm and 0.4 mm respectively.

Upon rupture of the diaphragm, a series of compression waves travel down the driven tube, which eventually coalesce to form a shock wave. Simultaneously, rarefaction waves are formed in the high-pressure region (driver). The fastest reflected rarefaction wave from the driver end catches the shock front and decays the pressure intensity of the shock front [32,33]. The wave profile evolved at the exit of the shock tube is shown in Fig. 2. The shape of the blast signal matches the typical pressure-time history of an air-blast explosion, given by the Eq. (3):

$$P(t) = P\left(1 - \frac{t}{t_d}\right)e^{\frac{-\alpha t}{t_d}} \tag{3}$$

where, t is the pressure wave duration time; P is peak overpressure, t_d is positive time duration and α is decay co-efficient.

The solid line shown in Fig. 2 is the pressure-time history recorded by pressure transducers (PCB113B23) S2, located at an offset distance of 0.2 m from the surface of the test sample. By observing the pressure profile, two distinctive shock fronts (jump) are identified. These vertical jumps correspond to the incident and reflected shock fronts. Response time of the rarefaction waves is significant in the formation of the blast wave [34], which eventually decides the blast wave parameters. The wave pulse generated from the shock tube is characterised by 'peak reflected overpressure' and 'positive time duration' as the blast wave parameters. It should be noted that, the pressure levels at the surface of the sample will be higher than the values recorded by S2. For all the test cases in the present study, peak reflected pressure (P^5) is considered as peak pressure value of the second jump and the positive phase duration (t_d) is the time taken for the reflected pressure (second jump) to decay to the atmospheric pressure levels (P_0). Further, the impulse is determined by calculating the area under the pressure-time curve (shaded portion in Fig. 2) over the positive phase duration (t_d).

The blast wave parameters obtained from the shock tube, are expressed in terms of equivalent charge weight of TNT (W) detonating at a stand-off distance (H) from the target surface, using charts developed by Kingery and Bulmash [35]. The air-blast parameter data of Kingery and Bulmash [35] are in graphical form in most of the available literature [20,36]. However, recently Shin et al. [37] has performed numerical modelling of the air-blast phenomenon using CFD analysis for scaled distance range of $0.0553 \leq Z < 40$ m/kg$^{1/3}$ and compared the results with the chart of Kingery and Bulmash. During this process, they have developed polynomial functions for a range of Z value and listed out the polynomial constant value for various blast parameters. With the help of these polynomial functions and constants, we have predicted 'Z' value (>1 m/kg $^{1/3}$) for the available blast parameters. Fig. 2 compares the blast wave profile for an explosion of 54.15 kg of TNT at a distance of 5.75 m, obtained from Kingery and Bulmash [35] chart with the one generated using shock tube (test no. RD45-1). It should be noted that, for specific 'Z' value, only the peak pressure and positive time duration match exactly. The impulse generated by the shock tube (area under the curve) is found to be slightly higher than the values predicted by the empirical charts. Similar test is repeated with different set of diaphragms (5 mm-2 mm and 2 mm-0.4 mm), to generate blast

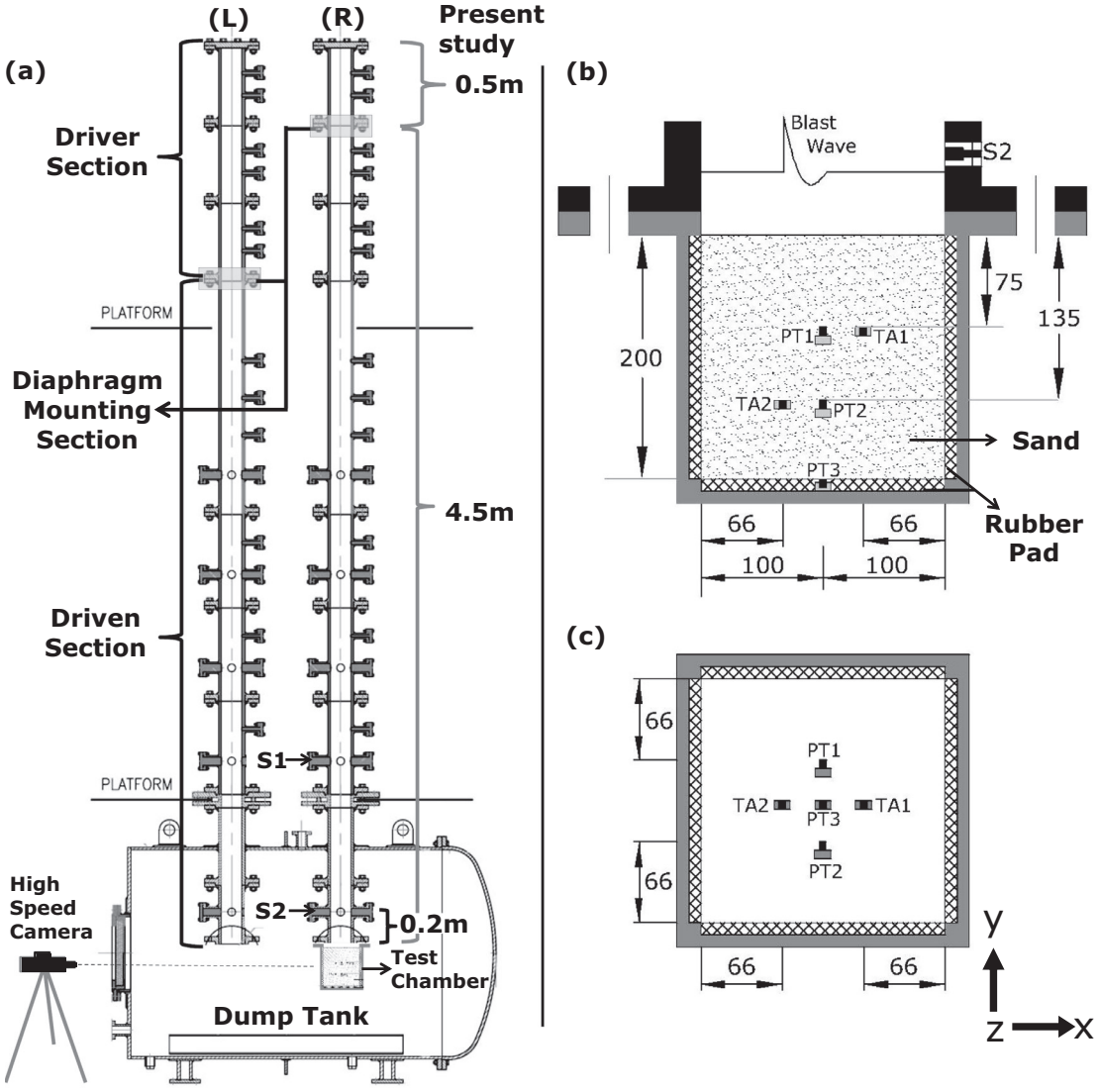

Fig. 1. Schematic diagram of the experimental setup. (a) Twin-shock tube, (b) sectional view of test chamber and (c) top view of test chamber.

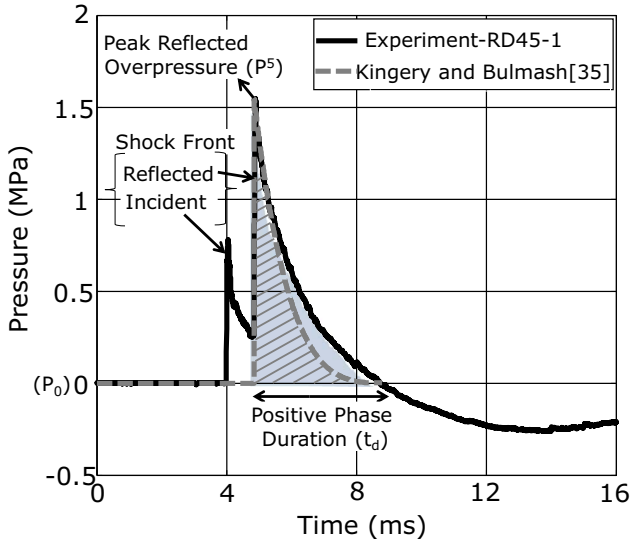

Fig. 2. Typical blast wave profile generated by the shock tube used in the present study.

Table 1
The shock tube blast parameters with corresponding TNT equivalents.

Test no.	Diaphragm type	Shock tube blast parameters		Equivalent TNT spherical charge		
		P5 MPa	Td ms	W kg	H m	Z m/kg1/3
RD45 Series						
RD45-1	4 mm-1mm	1.547	3.931	54.15	5.75	1.520
RD45-2		1.549	3.949	54.99	5.78	1.520
RD45-3	5 mm-2mm	1.428	4.161	60.51	6.12	1.559
RD45-4		1.371	3.865	44.61	5.60	1.579
RD45-5	2 mm-0.4 mm	0.755	2.951	11.3	4.30	1.916
RD45-6		0.745	3.343	16.61	4.90	1.920
RD45-7	5 mm-2mm	1.389	3.980	50.74	5.82	1.572
RD73 Series						
RD73-1	4 mm-1mm	1.487	3.384	33.64	5.00	1.549
RD73-2		1.62	3.391	37.13	5.00	1.499
RD73-3	5 mm-2mm	1.402	4.248	61.23	6.18	1.568
RD73-4		1.46	3.946	49.23	5.65	1.542
RD73-5	2 mm-0.4mm	0.731	2.614	9.56	4.10	1.932
RD73-6		0.783	2.881	10.98	4.20	1.890
RD73-7	5 mm-2mm	1.420	4.042	54.75	5.93	1.561

wave of different air-blast intensities. The shock tube blast parameters, along with their equivalent spherical TNT charge weights for different test cases are listed in Table 1.

2.2. Test chamber

The outlet of the driven section of the shock tube is connected to the test chamber, which is enclosed in the dump tank. The cross sectional and plan view of the test chamber is shown in Fig. 1(b) and (c) respectively. The test chamber is a cube-shaped steel chamber of size 250 mm × 250 mm, 225 mm in depth, with a wall thickness of 15 mm. To limit the wave reflections from the chamber walls, adjacent sides and the bottom face of the test chamber are provided with 10 mm thick rubber padding. These padded rubbers are expected to have lower impedance value, when compared to mild steel. For the test case which involves digital image correlation technique, one of the side walls of the test chamber is replaced by a 30 mm thick Plexiglas® window, which will facilitate in visualising and recording the particle movements.

Dry river bed sand is used to prepare the test specimen. The grain size of the sand particles varies from 0.075 mm to 2.36 mm and is classified as 'poorly graded' with symbol 'SP' as per Unified Soil Classification System (USCS). The grain size distribution and material properties of sand, used in the shock tube test experiments are shown in Fig. 3. A sand test specimen of 200 mm × 200 mm × 200 mm is prepared using the sand pluviation device. The sand pluviation technique is used to generate test samples of constant relative density (RD). The sand pluviation device consists of a hopper, an adjustable pipe and a diffuser. The overhead hopper is fitted with a flexible hose drain PVC pipe (adjustable in height between 100–500 mm), which is in turn connected to the diffuser. The sand diffuser is a hollow cylindrical pipe of 100 mm in length, with a 60° inverted cone, welded to the opening end. The sand grain particles are rained down from the hopper through the PVC pipe and exit into the test chamber through the diffuser. The diffuser is provided with a thin levelling rod which is set to a pre-marked level, prior to sand raining. The diffuser is held in upright position and is made to travel back and forth, such that uniform spread is obtained. Simultaneously, the diffuser is gradually traversed in the vertical direction as and when the sand bed level reaches the tip of the levelling rod, thus maintaining a constant height of fall. The height of fall determines the desired relative density of the sand deposit [38]. In the present study, two sand test specimens are prepared classifying themselves as medium dense and dense sand medium with a relative density of 45% and 73% respectively.

2.3. Instrumentation

2.3.1. Synchronised pressure and vibration measurement

As shown in the Fig. 1(b), three piezoelectric pressure transducers - PT1 (PCB113B23); PT2 (PCB113B22); PT3 (PCB113A24) and two triaxial accelerometers - TA1 (PCB356B11); TA2 (PCB356B11), are firmly embedded inside the test chamber using an adapter. It is assumed that the miniature sensors (PT and TA) embedded in the sand have minimum influence on the test signal (PCB Pressure sensors: 5.5 mm diameter × 37.5 mm length, with a mass of 6 g; PCB miniature Triaxial accelerometers: 10.2 × 10.2 × 10.2 mm, with a mass of 4 g). The triaxial accelerometer is composed of three uniaxial piezo-resistive accelerometers mounted orthogonal to each other. The TA is mounted such that the y-axis of the sensor is aligned vertical along the shock tube axis. The TA is used to distinguish blast wave induced vibrational activity in the lateral (x-z-axis) and longitudinal directions (y-axis). Piezoelectric pressure transducers are used to measure the dynamic pressure caused due to the stress waves. The wave propagation in the sand deposit is assumed to be symmetric along the shock tube axis and hence each pair of sensors (PT and TA) are located at depth of 75 mm and 135 mm respectively, from the top surface of the sand bed (shown in sectional view in Fig. 1(b)). PT and TA are located at 66 mm (one-third of sample dimension) from the side wall of the test chamber (shown in top view in Fig. 1(c)). A third pressure sensor PT3 is located at the centre of the bottom plate of the test chamber. The pressure transducers PT1 to PT3 record pressures, resulting from both the solid phase (stress transfer through particles) and gaseous phase (entrained gas). PT and TA transducers are simultaneously triggered by a signal from S2 sensor, which is closest to the surface of the sand bed. Yokogawa DL750 Oscilloscope is used to acquire accelerometer and pressure data, at a sampling rate of 100,000 samples per second.

2.3.2. Digital image correlation system

Digital image correlation (DIC) is an optical, non-contact based experimental technique that uses the digital images to determine the response of a system. ARAMIS-GOM [39], a commercial software is used for the DIC analysis in the present study. DIC method operates on the set of digital images of sand sample captured during undeformed and deformed states. The speckled images are divided into number of sub-images (facets). Facets track the characteristic features of the speckle pattern during loading. A displacement field is then computed and axial strain is averaged over a set of facets. The photograph of the test chamber with one of the side walls having a Plexiglas® window is

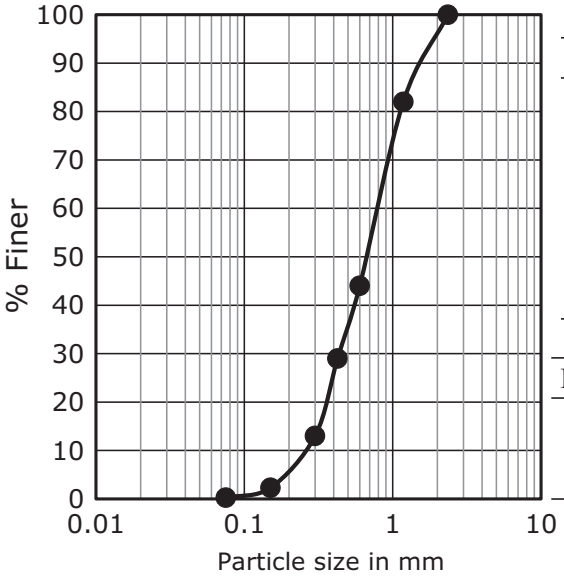

Parameter	Quantity
D_{10} (mm)	0.26
D_{50} (mm)	0.70
C_u	3.07
C_c	0.96
e_{max}	0.90
e_{min}	0.53

Drop Height	RD (%)
10 mm	45
20 mm	73

Fig. 3. Grain size distribution curve and gradation properties of the sand used in the present study.

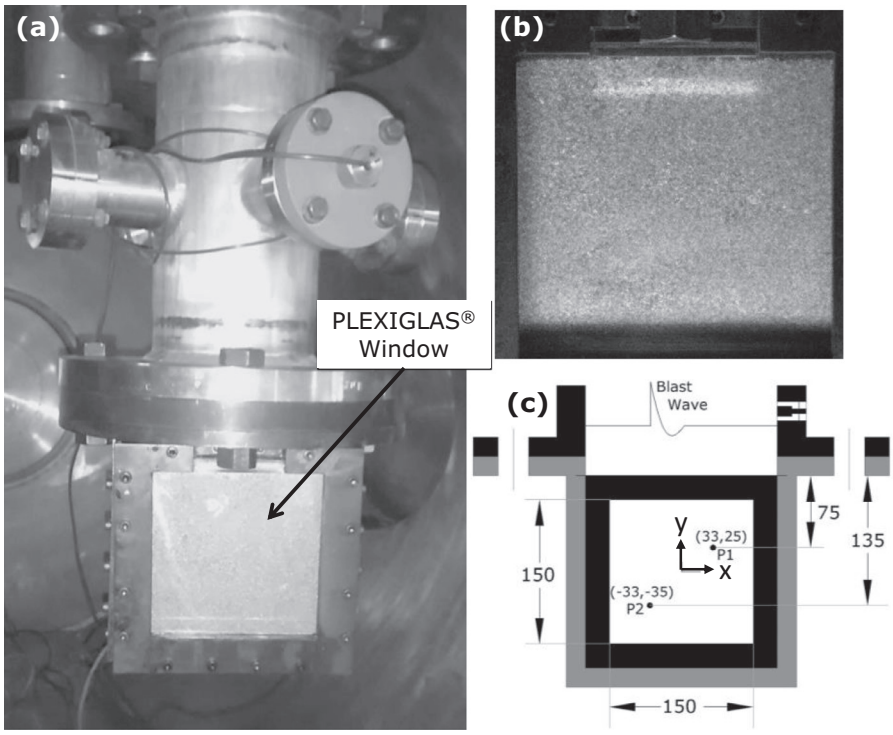

Fig. 4. A photograph of the test chamber. (a) A view of the test chamber with the dump tank door open, (b) speckle pattern generated by sand particles and (c) schematic diagram of the test chamber.

shown in Fig. 4(a) and the speckled image is shown in Fig. 4(b).

Upon blast impact, the speckle pattern generated by the sand particles undergoes transformation which is captured using high speed camera (Phantom V710). The optical axis of the camera is aligned perpendicular to window of test chamber and the camera position with respect to the sample is calibrated using a planar calibration target. The target used in the present study is 10 × 10 grid with 10 mm spacing. Built-in correlation algorithm available in Aramis is used for the analysis. Images are captured at high sampling rate (12,000 frames per second) to improve the accuracy of test results. The resolution of the captured image is 480 × 480 pixels. The sample surface illuminated with a tungsten-halogen light source generated a short exposure time of 82 μs. Images are processed using 19 × 19 pixels square facets, 9 pixels facet overlap with approximately 530 measuring points. A total of 100 sequential images captured during the test time, are selected for the DIC analysis.

In Fig. 4(c), two reference points, P1 and P2 are identified on the glass window. The location of P1 and P2 corresponds to the projection of transducer TA1 and TA2 on the window pane, which help us to validate DIC results against the physical measurement data. The absolute displacement of these two coordinate points is monitored by measuring the displacement between successive DIC interrogation windows, containing P1 and P2.

3. Experimental test program

The compressed gas driven shock tube is assembled with a configuration as mentioned in Section 2.1. The shock tube is operated using high pressure compressed Helium gas in the driver section and air at atmospheric pressure in the driven section. The blast experiments of varying intensities are carried out using diaphragms of 4 mm-1 mm (4 mm thick diaphragm with a 1 mm deep v-groove), 5mm-2 mm and 2mm-0.4 mm on medium dense (RD45 series) and dense sand samples (RD73 series). The blast parameters obtained for different input blast intensities are mentioned in Table 1.

Based on the measurement technique, test data results are analysed in three parts: (1) the propagation and attenuation of blast induced stress waves are analysed using the signals recorded from pressure transducers; 6 test run data are identified for each specimen (RD45-1 to 6 and RD73-1 to 6), (2) the vibration and particle velocity are measured using embedded triaxial accelerometers; two sets of data belonging to different scaled distance ranges are available for medium dense (RD45-1,2 and RD45-5,6) and dense (RD73-1,2 and RD73-5,6) sand samples and (3) the strain induced in medium dense and dense sand deposits are estimated using 2D-DIC system (RD45-7 and RD73-7).

4. Experimental results

4.1. Blast wave induced stress wave

The results of the experiments involving the measurement of stress (pressure) waves in sand medium is presented in this section. Two typical wave forms are illustrated in Figs. 5 and 6 for the test cases with medium dense (RD45-1,2) and dense (RD73-1,2) samples. The pressure-time history data are recorded from embedded pressure transducers (PT1-PT3). The figures also show pressure signal recorded by transducer S2, which is the closest port available from the sand surface and the signal recorded on S2 may be regarded as the applied blast loading.

Referring to the pressure profile in Figs. 5 and 6, the stress wave induced in the sand is characterised by the presence of instantaneous jump and thereafter the pressure is gradually increased to a peak value and then decreases immediately, which is followed by undular jumps, reducing the pressure levels to atmospheric values. As mentioned earlier, the pressure transducers embedded in the sand deposit measure both the stress transferred through the solid particles and the static pressures in the gaseous phase. Upon blast wave impact, the energy is released in the sand medium either as a stress wave or a shock wave, depending on the intensity of the blast and the impedance of the medium. During the initial phase, an abrupt compaction of the sand particles takes place at the surface, which leads a steep rise (jump) in pressure. The leading stress wave is followed by a turbulent gas flow. The gas permeates through the pores in sand medium, which is responsible for the gradual increase in the pressure, rising to the peak value and then decreases over a period of time. A very similar observation was made in study of buried blast loading [34]. Hence, the characteristic feature of the stress wave induced in the sand is to be

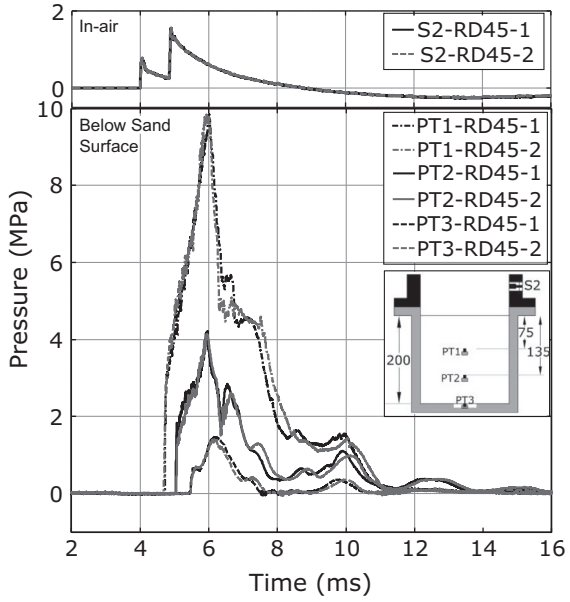

Fig. 5. Pressure-time waveforms recorded in medium dense sand sample.

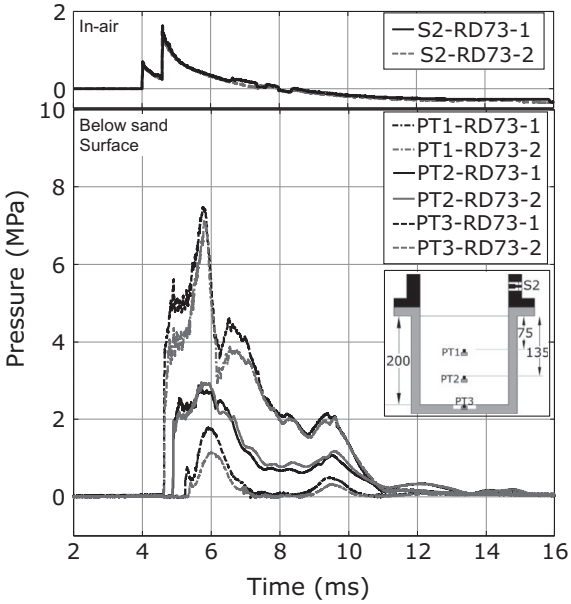

Fig. 6. Pressure-time waveforms recorded in dense sand sample.

attributed to both, the effective stress transfer through particle-particle contact and turbulent gas filtration process.

For a similar air-blast loading, the peak pressure values measured in sand specimen of medium dense are found to be higher than the dense specimen. Further, it is observed that the pressure measured at PT1 (P_d) is amplified multiple times of the peak blast overpressure (P^5) and subsequently pressure values are found to attenuate rapidly with depth. There exist similar as well as contrary outcomes in the previous studies. Akai et al. [24] have reported immediate attenuation of the pressure upon blast wave interaction with the surface. That is, the non-dimensional peak pressure value (P_d/P^5) was found to be lower than 1. However, this is not the case always. As observed in the present study, the pressure value might get amplified higher than the peak blast overpressure and then starts to attenuate in the medium. Experimental evidences on stress enhancement are available when compressible foams [40], porous textile layer [41,42] and sand deposits [43] were used as protective layer. The stress enhancement in cellular and porous material can occur when high intensive blast pulse is applied over a certain duration. The stress amplification in the medium is due to the formation of the shock wave due to sudden densification of the compressible medium [44]. The jump response observed in the stress wave trajectories of the present study are quite comparable to the characteristic feature of a shock. Hence, the stress enhancement is significant in the medium dense sand specimen (RD45) which contribute to a higher peak pressure when compared to the dense sand specimen (RD73), which is likely to undergo less densification.

As we observe the signals of embedded pressure transducers, the rise time for the pressure wave to attain its peak intensity decreases with the depth. The "rise time" is defined as the duration between the arrival time instances of the wave front to the time taken to attain the peak value. For a typical case of medium dense sample (RD45-1 in Fig. 5), the rise time is measured to be 1.295 ms, 0.893 ms and 0.666 ms, at a depth of 75 mm, 135 mm and 200 mm from the impact surface respectively. The passage of stress wave would have resulted in volumetric compressibility of the void space thereby restricting the flow of the entrained gas along the depth of the sample. In a compressed stratified layer of sand, the intensity of stress wave decreases with the depth and likewise the gas mass flow rate also varies along the depth. It is interesting to note that, though there is a time difference between arrival of the stress wave at PT1 and PT2, the peak value of the stress wave is reached at the same instance of time. The gas pressure steadily decreases until it encounters any reflected wave fronts.

The above experiments are repeated for different air-blast intensities. Results similar to those presented above are obtained. The maximum peak pressure values recorded from these tests are listed in the columns of peak pressure of Table 2.

4.2. Stress wave propagation and attenuation

Upon the blast wave impact on the surface, the compressive stress wave with an instantaneous rise propagates through the sand medium. The arrival time of the wave front is determined by calculating the duration between the impact time and the rising point of the stress wave signal. Since no sensors are mounted on the surface, the impact time is indirectly measured from transducers mounted in the shock tube. The velocity of the incident shock front is obtained from the arrival time of the incident shock wave recorded at S1 and S2. The impact time is calculated by from the offset distance of S2 and the velocity of the incident shock wave. The plot of arrival time of stress wave versus depths for medium dense (RD45) and dense (RD73) sand samples are shown in Fig. 7(a) and (b) respectively. The propagating stress wave velocities are obtained by a linear fit of dataset belonging to different category of scaled blast distance (Z). The slope of these lines gives us the propagating wave velocity in the medium. It is of interest to speculate the impact time by extrapolation of the lines towards zero value (depth and time). The results are satisfactory with all the lines pointing exactly towards the origin. The propagation velocity of stress wave is found to decrease with the increase in the scaled blast distance. The velocities with which these waves propagate, depends on the blast intensity and the properties of propagating medium. It has been shown experimentally for a similar scaled distance value, that the stress wave velocity is found to be propagating at higher velocity in the specimen having higher impedance value (ρ. c).

The peak pressure data recorded from the three embedded pressure transducers for different air-blast intensities is shown in Fig. 8(a). The peak pressure values in sand ranges from 10 MPa to 1 MPa. Notably, irrespective of the initial relative density of the specimen the peak pressure values are found to decrease sharply with depth. In order to obtain the non-dimensional form of the peak pressure (P_d) and distance (d), the former is divided by the peak overpressure (P^5) of the applied air-blast wave and latter is divided by scaled distance (Z). The non-dimensional peak pressure distribution in medium dense and dense sand for different blast intensities is shown in Fig. 8(b). The data points

Table 2
Summary of the experimental results for medium dense and dense sand samples.

Output values	Peak pressure (embedded) Pd			Propagation velocity	Peak acceleration		PPV
Test no.	d1 (MPa)	d2 (MPa)	d3 (MPa)	Vp (m/s)	d1 (g)	d2 (g)	d1 (m/s)
RD45 Series (Medium dense sand): Impedance (ρ.c = 177.82 kPa.s/m)							
RD45-1	9.83	4.21	1.44	168.30	747.85	688.40	2.199
RD45-2	9.82	4.12	1.39	166.90	737.70	668.70	2.178
RD45-3	9.56	3.73	1.28	153.40	–	–	–
RD45-4	10.04	3.75	1.79	155.50	–	–	–
RD45-5	5.26	2.58	0.78	125.80	406.05	356.11	1.421
RD45-6	5.48	2.67	1.04	118.10	417.25	320.83	1.403
RD73 Series (Dense sand): Impedance (ρ.c = 206.67 kPa.s/m)							
RD73-1	7.48	2.88	1.78	200.90	581.81	513.41	1.507
RD73-2	7.12	2.95	1.15	215.40	554.88	490.05	1.452
RD73-3	6.7	2.28	1.09	159.50	–	–	–
RD73-4	6.37	2.48	1.29	156.00	–	–	–
RD73-5	3.22	1.63	0.75	140.10	333.15	–	1.087
RD73-6	3.09	1.75	0.79	124.00	316.63	–	1.075

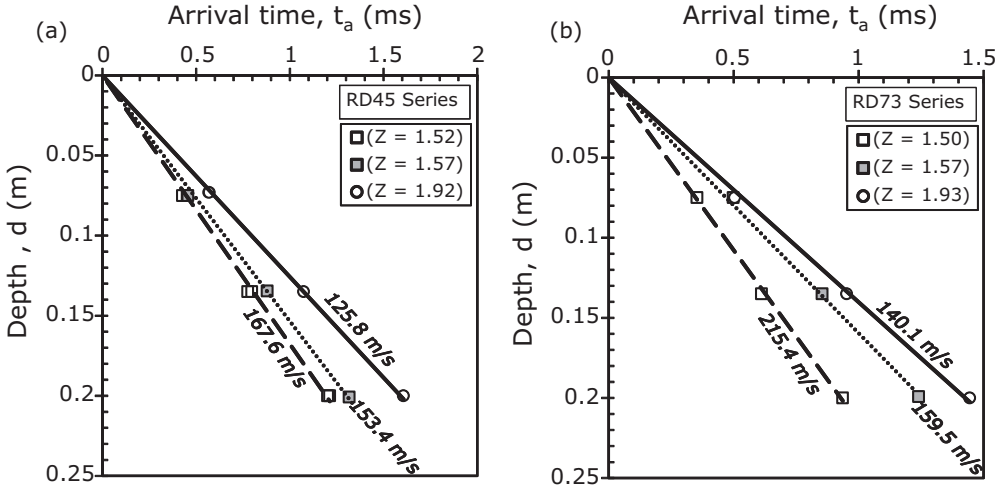

Fig. 7. Plot of arrival time of stress wave versus depths. (a) Medium dense sand (b) dense sand.

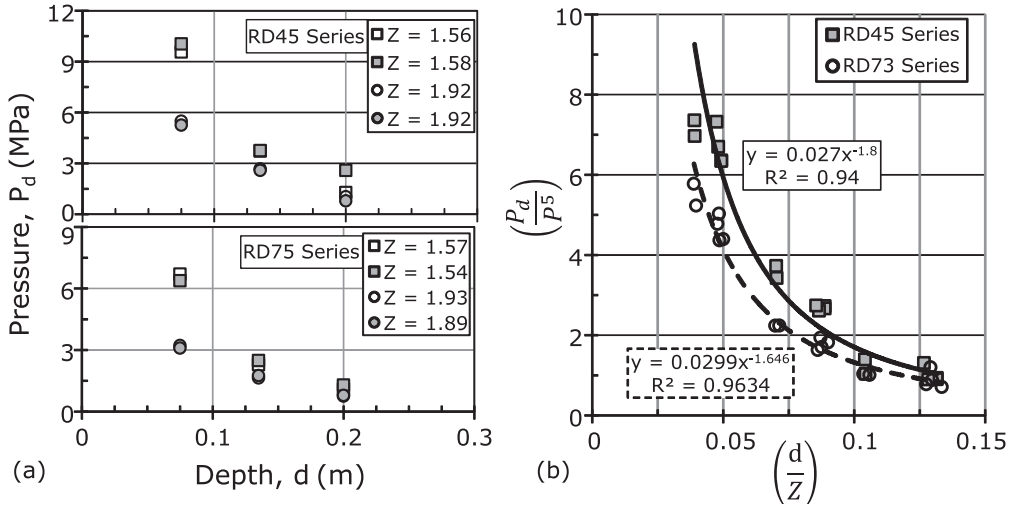

Fig. 8. Peak pressure distribution in sand. (a) Pressure versus along the sample depth for RD45 and RD73 and (b) peak pressure attenuation in sand.

for the respective test series are provided with power-law regression fit, as most common expression (Eq. (1)) for pressure attenuation with scaled distance. The equation of the line and corresponding R^2 values are highlighted in the plot area. The attenuation coefficient, 'k' (exponent term) for the medium dense sand and dense sand is found to be 1.80 and 1.64 respectively.

A more explicit and generic expression for different blast intensities is generated by multiplying the parameters (non-dimensional pressure

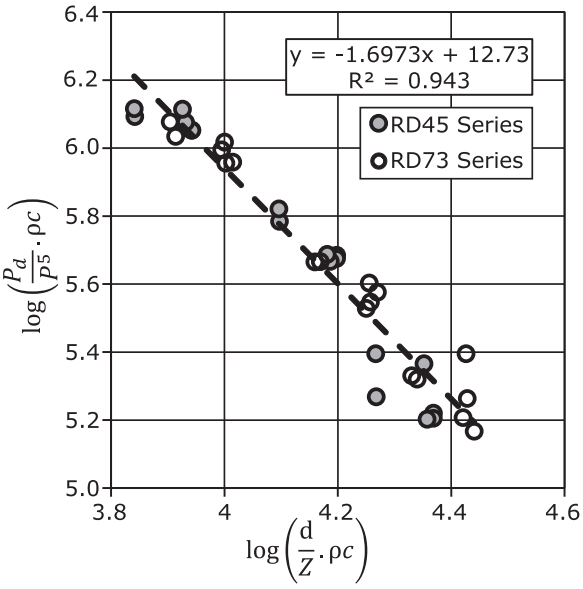

Fig. 9. Plot showing normalised pressure parameter versus normalised depth parameter.

and distance values) with the impedance value of the sample and represented in logarithm scale of base 10. The normalised pressure data points recorded from all the experiments (test series RD45-1 to 6 and RD73-1 to 6) are shown in Fig. 9. Consequently, a direct relationship is established by plotting a linear least-squares regression line, as shown in Eq. (4). The scatter of the normalized data points shows a reasonable average prediction, with more than 90% of the data points are well within a band of ± 30% offset value from the dotted line.

$$log\left(\frac{P_d}{P^5}.\,\rho c\right) = -1.6973\ log\left(\frac{d}{Z}.\,\rho c\right) + 12.73 \tag{4}$$

It should be noted that the present study considers only limited number of scaled distances and the above equation is valid for prediction over a shallow depth of dry sand deposit without any effect of confinement pressure.

4.3. Blast wave induced vibration

As discussed in the previous sections, when blast wave strikes the surface, high intensity stress wave is induced in the sand medium, which is followed by rapidly expanding gas at high pressure. The passage of stress wave and gas flow will induce vibration in the sand medium, which is composed of body waves and surface waves [45,46]. The effect and implication of compressional body waves alone is

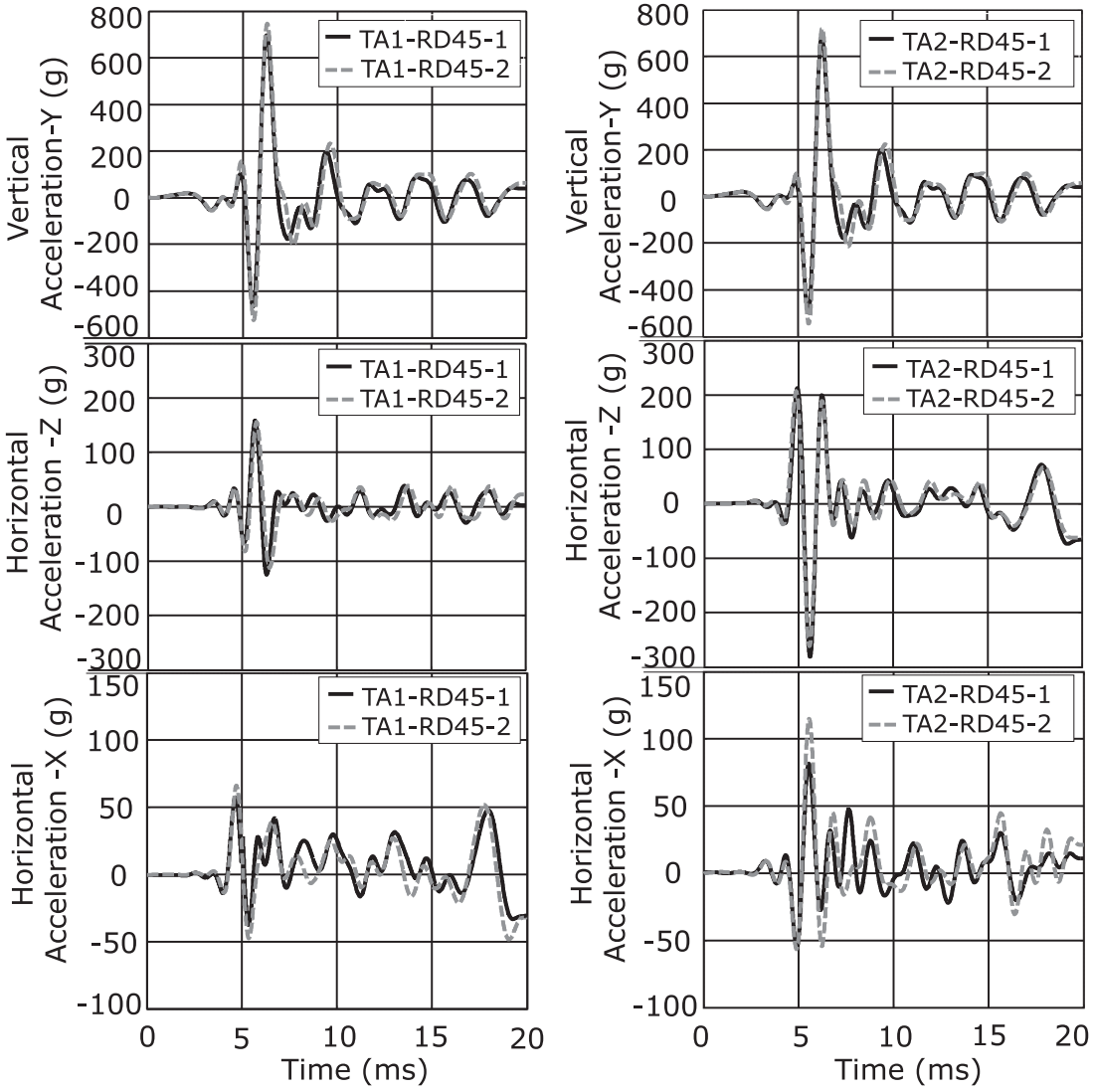

Fig. 10. Acceleration-time response along x, y and z direction of medium dense sand sample (Left panel: signal recorded at 75 mm; Right panel: signal recorded at 135 mm).

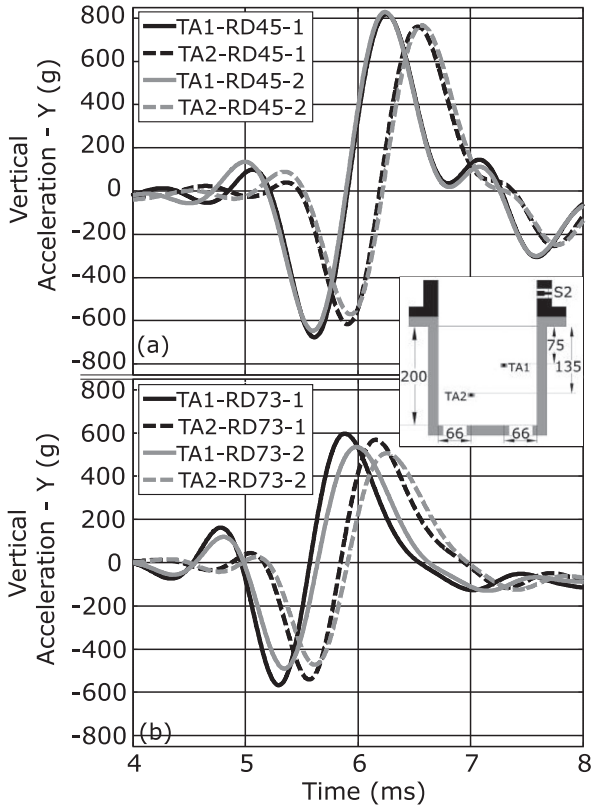

Fig. 11. Plot compares the y-axis accelerometer response. (a) Medium dense sand and (b) dense sand.

considered in the experimental investigation, but most significant in the direction of blast wave impact. Though, propagating stress wave is believed to be travelling in 1-dimensional (in the present study), slight disturbance will be observed in other dimensional space. The triaxial accelerometers are used to measure the disturbance and it is commonly expressed in peak particle acceleration (PPA) and peak particle velocity (PPV). The energy transmitted in the form of vibrational waves is often denoted as PPV and has always been quantified with a meaningful relationship with the scaled distance of the explosion. It should also be noted that only selected representative acceleration/velocity responses are presented herein. As the testing was progressed for different test cases, accelerometer located at TA2 became inoperative for certain cases of dense sand samples.

The acceleration-time series waveforms recorded along the three coordinate axes for the two experiments performed using similar blast intensities are shown in Fig. 10. The wave forms are obtained at depth of 75 mm and 135 mm from the blast wave impact surface of medium dense sample (RD45-1,2). Very good repeatability is shown in signal measurements. The vertical and horizontal acceleration signals shown in Fig. 10 are filtered using a low-pass Butterworth filter with a cutoff frequency of 1 kHz. Referring to the left panel of Fig. 10 (signals from TA1), the maximum horizontal component is less than half the magnitude of the maximum amplitudes of vertical component of the acceleration. However, significant amplification is observed in horizontal-x and z signals recorded at TA2 when compared to signals recorded at TA1. The exact reason for the large transverse acceleration is unknown, these signals can be possibly due to the noise characteristics. The present study restricts the analysis to vertical acceleration in Y-direction.

To get more insights into the vertical acceleration data, signals of TA1 and TA2 are plotted in the same graph over the test time (time scale ranging from point of arrival to the time taken to complete the first full cycle of vibration). The vertical acceleration response for medium dense and dense sand sample is shown in Fig. 11. The amplitude of the acceleration is found to decrease with depth and the peak amplitude is noticeably higher in the medium dense sample, when compared to the dense sample (as seen in stress waves).

The velocity–time profiles are obtained by integrating the corresponding acceleration signals using a MATLAB function. The velocity profiles generated in medium dense and dense sand for different blast intensities are shown in Fig. 12(a) and (b) respectively. The velocity signal profiles shown in Fig. 12 for different cases correspond to the acceleration response of Y-component of TA1, which is relatively close to the blast-sand surface interaction. The mean peak particle velocity (PPV) is determined for respective test cases. Best-fit least-squares equations are developed for calculated PPV in terms of scaled distance (Z), for the medium dense (RD45) and dense (RD73) sand specimen. The best fit curve is shown in Fig. 13 and the generalised equations obtained in the form of Eq. (1) are shown in Eqs. (5) and (6). The constant C and k depend on the material properties (impedance value) of the ground conditions [47].

$$PPV = 4.80\left(\frac{H}{W^{1/3}}\right)^{-1.88}\ \text{m/s} \qquad \text{medium dense sand} \tag{5}$$

$$PPV = 2.61\left(\frac{H}{W^{1/3}}\right)^{-1.36}\ \text{m/s} \qquad \text{dense sand} \tag{6}$$

4.4. Estimation of blast induced displacement and strain fields

This section discusses DIC results of two blast impact tests on medium dense (RD45-7) and dense sand (RD73-7) medium. The downward and upward movement of the sand particles were evident during high speed photography. An instant displacement and strain field are obtained by analysing the high-speed images using DIC algorithms.

Displacement contour fields generated for a medium dense sand deposit (RD45-7) are presented through a series of images in Fig. 14(a). A snapshot of the original image considered for the DIC analysis is superimposed on one of the contour image. The displacement contours are computed at a time interval of 83.32 μs and a maximum value is captured at 2.51 ms from the trigger event (at 4 ms). The peak pressure value of stress waves is observed around 6 ms (refer Fig. 5), which is 2 ms from the trigger point. This reveals that, upon passage of the stress waves, the sand bed is susceptible to particle rearrangement. The particle displacements are observed to be predominant in the middle portion of the specimen, which are highlighted by blue density contours. The displacement of coordinate points, P1 and P2 are plotted over test time duration in Fig. 14(b). The locations of points P1 and P2 are the projection of the buried accelerometers. The data points highlighted in the red corresponds to the images shown in Fig. 14(a). The maximum displacement for the particle located at P1 and P2 is found to be −1.613 mm and −1.347 mm. The particle motions near the embedded accelerometers are described by acceleration–time series in Fig. 11(a) of Section 4.3. The displacement value is numerically determined by integrating twice the acceleration signal. The peak displacement for P1 and P2 by direct integration is found to be −1.587 mm and −1.457 mm, which is close to the values obtained through optical methods.

The infinitesimal strains generated in the sample are computed using DIC algorithm available in GOM-ARAMIS [30]. The strain contours over the lateral surface area of the test specimen are shown in Fig. 15(a), RD45 and Fig. 15(b), RD73. The images of strain field shown for medium dense and dense sand specimen are captured at 2.51 ms and 2.55 ms respectively from the time of the trigger. Plots in Fig. 15 shows the strain profile as a function of depth. The specimen can be divided into two parts, upper half where positive strain is observed and the lower half with predominantly negative strain. Maximum strains are observed in the upper half of the specimen, which is close to the surface of blast interaction. The regions immediately adjacent to the surface are

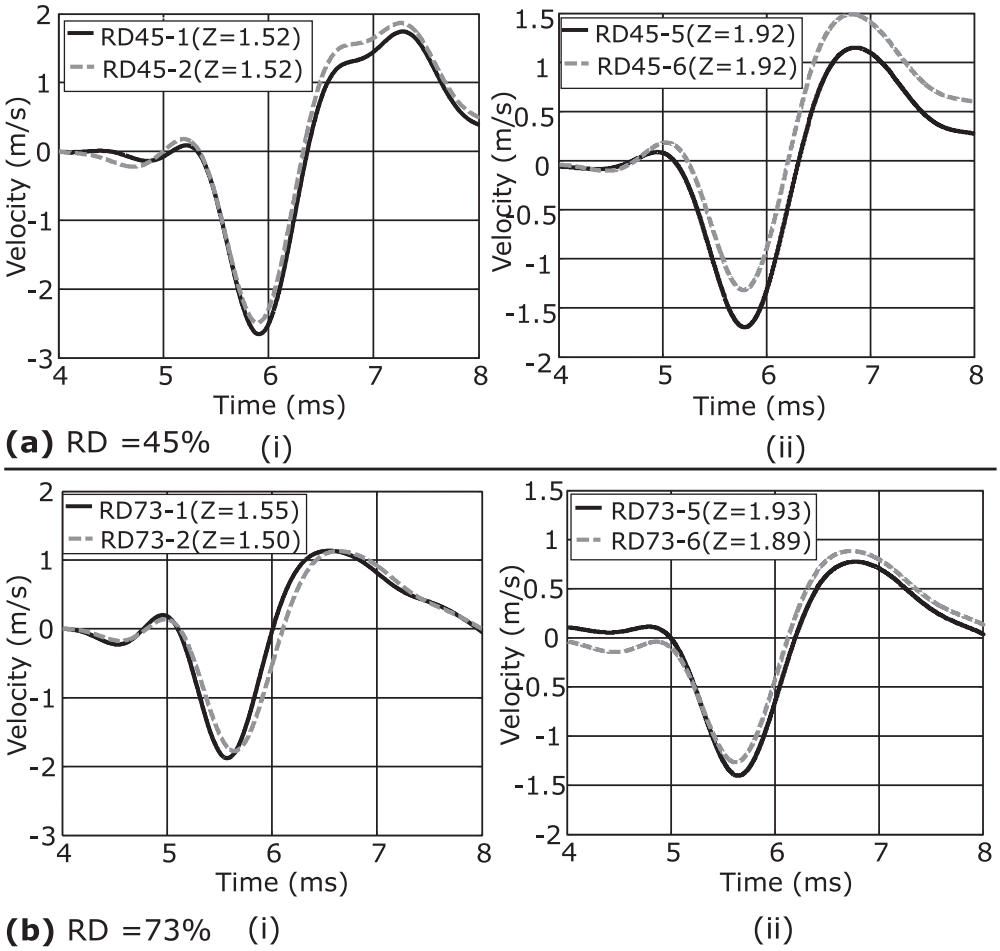

Fig. 12. Velocity-time response for different scaled blast distance. (a) Medium dense sand (b) dense sand.

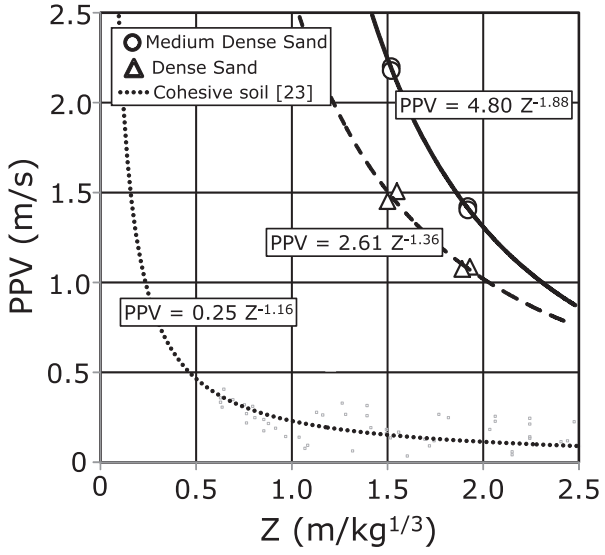

Fig. 13. Plot showing relationship between peak particle velocity and scaled distance.

highly compressed due high pressure resulting from stress enhancement and gas filtration process. It is also noteworthy that the relatively large negative strains are formed in the lower half portion. This dilative strain is due to propagation of reflected stress wave from the bottom of the test chamber. The magnitude of the strain is lower in dense sand when compared to medium dense sample. The sand particles in dense sample are packed closely prior to blast impact, restricting any further movement of the particles due to the compaction wave front. Thus, one can assume that there is minimum deformation in the denser sample. One of the major disadvantages of using DIC method to measure local strain and displacement is that the measurement is restricted to 2-dimensional space, while there can be significant movement in the lateral direction as well.

5. Discussion

In this section, we present and compare the shock tube test results with the data available in the literature on air-blast study using explosives. A small-scale air-blast experiment was performed by Busch et al. [23] using TNT weight ranging from 0.9 g to 100.9 g on a cohesive soil medium. A direct comparison of the test results with the present study is not possible, due to the variability in the different parameters of the test conditions.

$$PPV = 0.25\left(\frac{H}{W^{1/3}}\right)^{-1.16} \text{ m/s} \qquad \text{cohesive soil [23]} \tag{7}$$

The variation of PPV data points of Busch et al. [23] is shown in Fig. 13 and the attenuation trend lines of PPV is described by Eq. 9. The data points are found to be more scattered away from the present study values. Use of cohesive clay sample could be a possible reason. Moreover, the formula for estimating scaled distance (Z) differs from the present study. Busch et al. [23] have defined the altitude 'H' as the distance of the buried sensor from the blast source, i.e., it includes the air standoff distance plus the depth of burial of the sensor. Nevertheless, we find that the present study results are in meaningful agreement with the trends obtained from the tests using real explosives. Mechanical densification of sand particles becomes increasingly cohesive with the applied pressure [48]. Increase of 'ρ' and 'c' in the sand deposit has

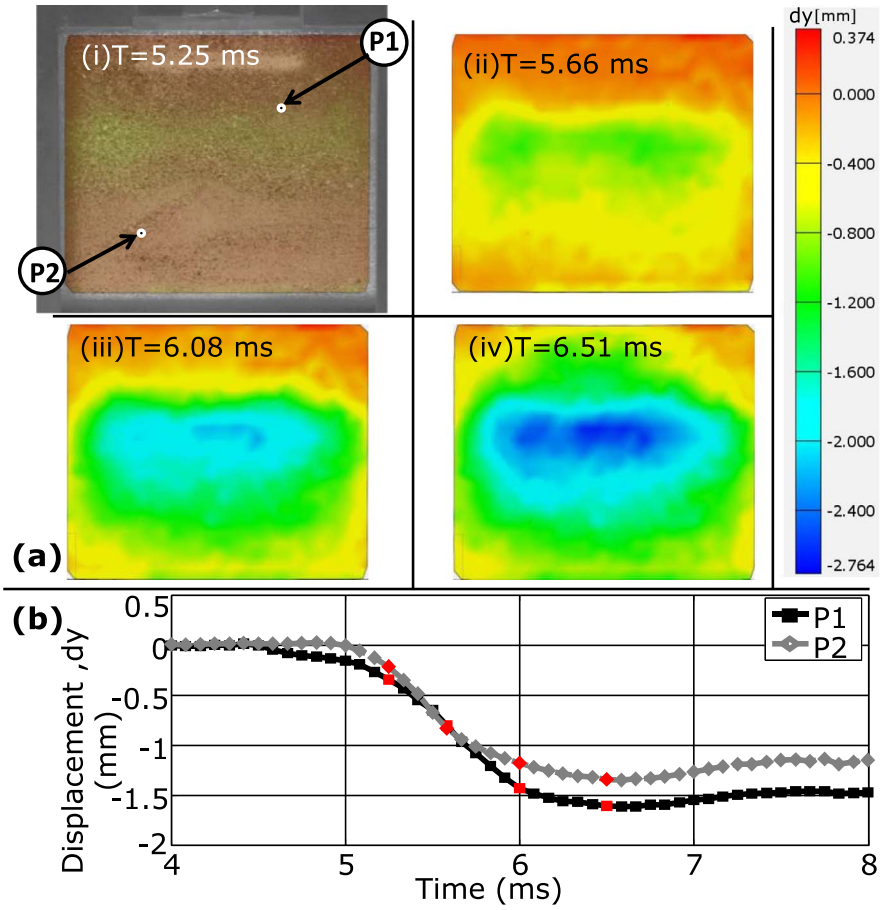

Fig. 14. DIC analysis results. (a) Displacement contour at t = 5.25 ms, 5.66 ms, 6.08 ms and 6.51 ms and (b) displacement versus time for coordinate P1 and P2.

confirmed the increase of cohesive forces because of particle–particle interactions. With the increase in impedance (ρ.c) value, the constants C and k are found to decrease, which ultimately reduces PPV value. An extended comparison between trend line of Busch et al., [23] and the present study has concluded that the impendence value play a significant role in the estimation of the blast response parameters in the soil sample.

In the present study, we have used compressed gas-driven shock tube to generate air-blast wave. The maximum peak overpressure achieved using the gas-driven shock tube is 1.5 MPa. The pressure levels are found to be lower and does not include the effect of crushing, particle breakage and the thermal radiation resulting from blast interaction. However, the shock tube based method enables us to study the air-blast effects on sands when exposed to low intensity blast waves. This study has shown a detailed investigation on representative smaller size sand samples. The same procedure can be extended further on larger soil deposits. The main limitation of using gas-driven shock tube is the inability to generate higher overpressure [34], and this can be achieved using detonation-driven shock tube.

6. Summary and conclusion

The general objective of this study is to observe the characteristic response of sand under different air blast intensities and this is demonstrated with the help of a shock tube. The shock tube simulates blast waves in a controlled laboratory environment; air-blast wave loading generated is then characterised with TNT equivalent of an explosion. The experiments are performed over dry medium dense (RD = 45%) and dense (RD = 73%) sand specimens. Pressure transducers and accelerometers are positioned in the sand specimens to measure the intensity of pressure waves and vibrational amplitudes. Synchronised pressure and accelerometer measurements have enabled a thorough investigation of stress wave induced vibrations. Finally, digital image correlation technique is used to obtain displacements and strains induced in the sand deposits.

Immediately after the blast wave strikes the sand surface, a high intensity compressive stress wave is generated in the sand medium. The layer of sand just below the surface is abruptly compacted, which leads to stress enhancement, especially with the sample of relatively low relative density. The stress transfer through sand particles and the expansion of high pressure gas through sand media plays an important role in the formation of stress waves. Peak stress wave pressures in sand and peak particle velocity (PPV) are observed to decrease with increase in the cube root of the scaled distance of an air-blast. Dimensionless parameters are identified to predict the peak pressure and PPV in medium dense and dense sand corresponding to the scaled distance range of 1.52–1.93 m/kg$^{1/3}$ respectively. Incremental displacement of the sand deposit acquired through DIC showed that the displacement patterns are well comparable with the direct physical measurements. The strain field obtained from the image analysis has revealed large magnitude of compressive strains in the layers adjacent to the blast impact.

Based on the experimental results, an empirical equation has been developed as a function of scaled distance to predict peak pressure and peak particle velocity in sands. The prediction of these parameters will help us to evaluate the potential of granular medium like sand in mitigating the air-blast effects and can aid in the design of protective structures. The experimental investigation presented in this paper is limited to a very small range of scaled blast distances. It is necessary to replicate the present study over a wide range of scaled distances and larger size samples (with and without confining pressure). To further demonstrate the bonding and cohesion effects, additional experiments

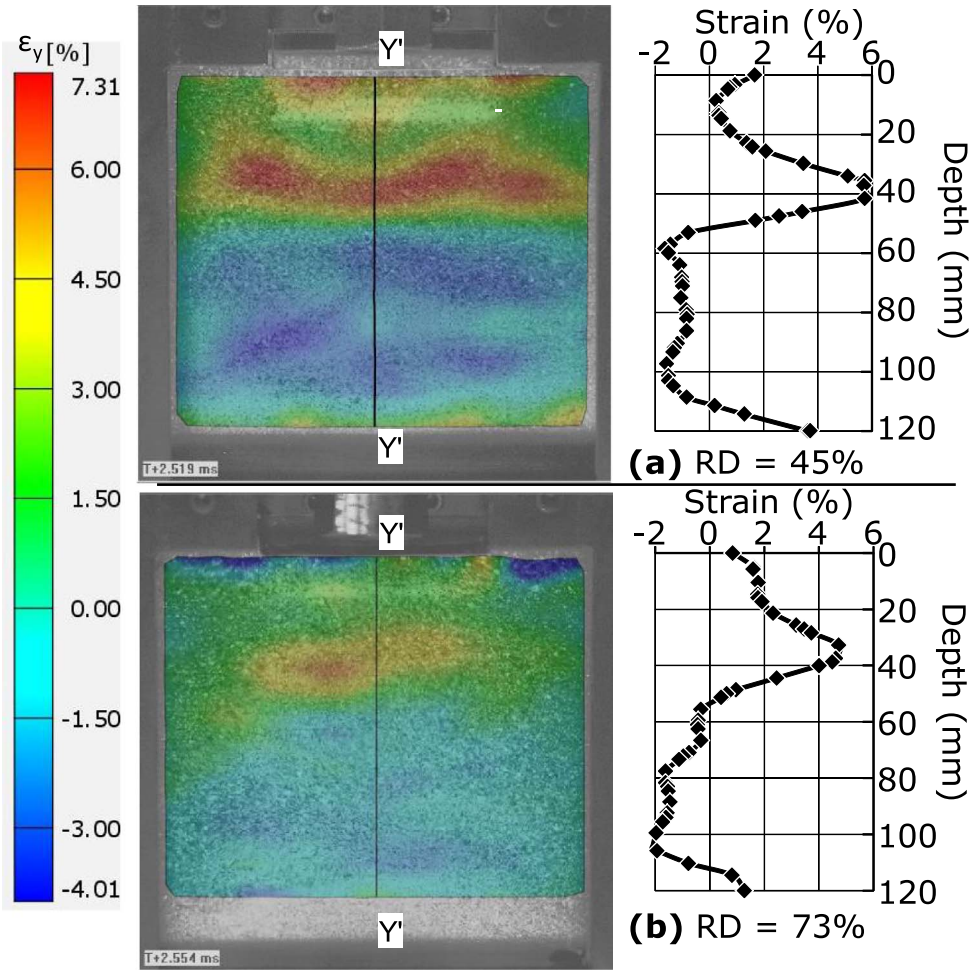

Fig. 15. Computed strain contour for (a) medium dense sand and (b) dense sand. (Plot shows variation of strain along Y'-Y' section).

need to be carried out on fine grained soils and cohesive clay samples.

Acknowledgements

The shock tube experiments were performed at Laboratory for Hypersonic and Shock Wave Research (LHSR) at Indian Institute of Science, Bangalore, the first author thank Prof. KPJ Reddy for agreeing to use their test facility. We acknowledge the efforts of colleagues and non-technical staffs in LHSR and Soil Mechanics Laboratory, at Indian Institute of Science. The work is supported by grants provided by DST, Govt. of India and International bi-lateral co-operation division, Indo-German (DST-BMBF) cooperation in civil security research (F. No. IBC/FR6/BMBF/CSR/R-03/2015).

References

[1] Scherbatiuk K, Rattanawangcharoen N. A hybrid rigid-body rotation model with sliding for calculating the response of a temporary soil-filled wall subjected to blast loading. Int J Impact 2011;37:11–26.
[2] Smith P. Blast walls for structural protection against high explosive threats: a review. Int J Prot Struct 2010;1:67–84. http://dx.doi.org/10.1260/2041-4196.1.1.67.
[3] Wu C, Hao H, Lu Y, Sun S. Numerical simulation of structural responses on a sand layer to blast induced ground excitations. Comput Struct 2004;82:799–814. http://dx.doi.org/10.1016/j.compstruc.2004.01.003.
[4] Alekseenko VD, Rykov G V. Experimental data on stress-wave parameters in the earth due to underground and surface explosions. J Appl Mech Tech Phys 1972;9:409–11. http://dx.doi.org/10.1007/BF00912739.
[5] William RP, Robert CB. Free-field ground motion induced by underground explosions. Albuquerque, New Mexico: Sandia Laboratories; 1975. SAND740252.
[6] Drake JL, Little CD. Ground shock from penetrating conventional weapons. Proceedings of the symposium on the interaction of non-nuclear weapons with structures. 1983.
[7] Fundamentals of protective design for conventional weapons TM5-855-1 US Department of the Army Technical Manual, USA Army Corps of Engineers; 1986
[8] Rinehart EJ, Welch CR. Material properties testing using high explosives. Int J Impact Eng 1995;17:673–84. http://dx.doi.org/10.1016/0734-743X(95)99890-4.
[9] Roy PP. Characteristics of ground vibrations and structural response to surface and underground blasting. Geotech Geol Eng 1998;16:151–66. http://dx.doi.org/10.1023/A:1008815023176.
[10] Wu C, Lu Y, Hao H, Lim WK, Zhou Y, Seah CC. Characterisation of underground blast-induced ground motions from large-scale field tests. Shock Waves 2003;13:237–52. http://dx.doi.org/10.1007/s00193-003-0212-3.
[11] Selig ET, Vey EE. Shock Induced Stress Wave Propogation in Sand. J Soil Mech Found Div 1965.
[12] Stoll RD, Ebeido IA. Shock Waves in Granular Soil. J Soil Mech Found Div 1965;91:107–26.
[13] Gu Q, Lee F-H. Ground response to dynamic compaction of dry sand. Géotechnique 2002;52:481–93. http://dx.doi.org/10.1680/geot.2002.52.7.481.
[14] Brown JL, Vogler TJ, Chhabildas LC, Reinhart WD, Thornhill TF. Shock response of dry sand.Albuquerque N.M: Sandia National Laboratories; 2007. Report SAND2007e3524. n.d.
[15] Yamamuro JA, Bopp PA, Lade P V. One-dimensional compression of sands at high pressures. J Geotech Eng 1996;122:147–54. http://dx.doi.org/10.1061/(ASCE)0733-9410(1996)122:2(147).
[16] Omidvar M, Iskander M, Bless S. Stress-strain behavior of sand at high strain rates. Int J Impact Eng 2012;49:192–213. http://dx.doi.org/10.1016/J.IJIMPENG.2012.03.004.
[17] Vivek P, Sitharam TG. The effect of spherical air blast on buried pipelines: a laboratory simulation study. Int J Phys Model Geotech 2017:1–11. http://dx.doi.org/10.1680/jphmg.16.00070.
[18] Baker WE. Explosions in air. Austin, USA: University of Texas Press; 1973.
[19] Kinney GF, Graham KJ. Explosive shocks in air. 2nd edition New York, USA: Springer; 1985. http://dx.doi.org/10.1007/978-3-642-86682-1.
[20] Smith PD, Hetherington JG. Blast and ballistic loading of structures. London, Great Britan: Butterworth-Heinemann; 1994.
[21] Leong EC, Anand S, Cheong HK, Lim CH. *Re*-examination of peak stress and scaled distance due to ground shock. Int J Impact Eng 2007;34:1487–99. http://dx.doi.org/10.1016/j.ijimpeng.2006.10.009.
[22] Ambrosini RD, Luccioni BM, Danesi RF, Riera JD, Rocha MM. Size of craters produced by explosive charges on or above the ground surface. Shock Waves 2002;12:69–78. http://dx.doi.org/10.1007/s00193-002-0136-3.

[23] Busch CL, Aimone-Martin CT, Tarefder RA. Experimental evaluation of cratering and ground vibration in clay soils subjected to explosive airblast loading. J Test Eval 2015;43:20130296http://dx.doi.org/10.1520/JTE20130296.
[24] Akai K, Hori M, Ando N, Shimogami T. Shock tube study on stress wave propagation in confined soils 1972;200:127–40.
[25] van der Grinten JGM, van Dongen MEH, van der Kogel H. A shock-tube technique for studying pore-pressure propagation in a dry and water-saturated porous medium. J Appl Phys 1985;58:2937–42. http://dx.doi.org/10.1063/1.335841.
[26] Sniekers RWJM, Smeulders DMJ, van Dongen MEH, van der Kogel H. Pressure wave propagation in a partially water-saturated porous medium. J Appl Phys 1989;66:4522–4. http://dx.doi.org/10.1063/1.343955.
[27] Smeulders DMJ, van Dongen MEH. Wave propagation in porous media containing a dilute gas–liquid mixture: theory and experiments. J Fluid Mech 1997;343:351–73. http://dx.doi.org/10.1017/S0022112097005983.
[28] Ben-Dor G, Britan A, Elperin T, Igra O, Jiang JP. Experimental investigation of the interaction between weak shock waves and granular layers. Exp Fluids 1997;22:432–43. http://dx.doi.org/10.1007/s003480050069.
[29] Britan A, Shapiro H, Ben-Dor G. The contribution of shock tubes to simplified analysis of gas filtration through granular media. J Fluid Mech 2007;586. http://dx.doi.org/10.1017/S0022112007006878.
[30] Vivek P, Sitharam TG. Shock wave attenuation by geotextile encapsulated sand barrier systems. Geotext Geomembranes 2017;45:149–60. http://dx.doi.org/10.1016/j.geotexmem.2017.01.006.
[31] Sundaramurthy A, Chandra N. A parametric approach to shape field-relevant blast wave profiles in compressed-gas driven shock tube. Front Neurol 2014;5:253. http://dx.doi.org/10.3389/fneur.2014.00253.
[32] Kleinschmit N. A shock tube technique for blast wave simulation and studies of flow structure interactions in shock tube blast experiments. Lincoln: University of Nebraska; 2011.
[33] Aune V, Fagerholt E, Langseth M, Borvik T. A shock tube facility to generate blast loading on structures. Int J Prot Struct 2016;7:340–66. http://dx.doi.org/10.1177/2041419616666236.
[34] Vivek P, Sitharam TG. Sand ejecta kinematics and impulse transfer associated with the buried blast loading: a controlled laboratory investigation. Int J Impact Eng 2017;104:85–94. http://dx.doi.org/10.1016/j.ijimpeng.2017.02.017.
[35] Kingery C, Bulmash G. Air blast parameters from TNT spherical air burst and hemispherical surface burst. Maryland, USA: US Army Armament Research and Development Centre; 1984.
[36] Needham CE. Blast waves (shock waves and high pressure phenomena). 1st Edition Berlin, Heidelberg: Springer; 2010. p. 49–50. http://dx.doi.org/10.1007/978-3-642-05288-0_1.
[37] Shin J, Whittaker AS, Cormie D. Incident and normally reflected overpressure and impulse for detonations of spherical high explosives in free air. J Struct Eng 2015;14:4015057http://dx.doi.org/10.1061/(ASCE)ST.1943-541X.0001305.
[38] Vaid YP, Negussey D. Relative density of pluviated sand samples. Soils Found 1984;24:101–5.
[39] GOM mbH. Aramis user's manual. Germany; 2009.
[40] Cooper GJ, Townend DJ, Cater SR, Pearce BP. The role of stress waves in thoracic visceral injury from blast loading: modification of stress transmission by foams and high-density materials. J Biomech 1991;24:273–85.
[41] Hattingh TS, Skews BW. Experimental investigation of the interaction of shock waves with textiles. Shock Waves 2001:115–23. http://dx.doi.org/10.1007/PL00004064.
[42] Skews BW, Bugarin S. Blast pressure amplification due to textile coverings. Text Res J 2006;76:328–35. http://dx.doi.org/10.1177/0040517506062264.
[43] Gelfand BE, Medvedev SP, Borisov AA, Polenov AN, Frolov SM, Tsyganov SA. Shock loading of stratified dusty systems.pdf. Arch Combust 1989;9:153–65.
[44] Li QM, Meng H. Attenuation or enhancement - A one-dimensional analysis on shock transmission in the solid phase of a cellular material. Int J Impact Eng 2002;27:1049–65. http://dx.doi.org/10.1016/S0734-743X(02)00016-7.
[45] Albert DG, Taherzadeh S, Attenborough K, Boulanger P, Decato SN. Ground vibrations produced by surface and near-surface explosions. Appl Acoust 2013;74:1279–96. http://dx.doi.org/10.1016/j.apacoust.2013.03.006.
[46] Yasui M, Matsumoto E, Arakawa M. Experimental study on impact-induced seismic wave propagation through granular materials. Icarus 2015;260:320–31. http://dx.doi.org/10.1016/j.icarus.2015.07.032.
[47] Kumar R, Choudhury D, Bhargava K. Prediction of blast induced vibration parameters for soil sites. Int J Geomech 2013;14:1–10. http://dx.doi.org/10.1061/(ASCE)GM.1943-5622.0000355.
[48] Piccolroaz A, Bigoni D, Gajo A. An elastoplastic framework for granular materials becoming cohesive through mechanical densification. Part I – small strain formulation. Eur J Mech - A/Solids 2006;25:334–57. http://dx.doi.org/10.1016/j.euromechsol.2005.10.001.